GEOPHYSICS, VOL. 80, NO. 2 (MARCH-APRIL 2015); P. E97–E110, 10 FIGS.
10.1190/GEO2014-0015.1

Rapid resistivity imaging for marine controlled-source electromagnetic surveys with two transmitter polarizations: An application to the North Alex mud volcano, West Nile Delta

Andrei Swidinsky[1], Sebastian Hölz[2], and Marion Jegen[2]

ABSTRACT

To image the internal resistivity structure of the North Alex mud volcano offshore Egypt, the marine electromagnetics group at the Helmholtz Centre for Ocean Research Kiel (GEOMAR) developed and conducted a novel transient marine controlled-source electromagnetic experiment. The system, which was specifically developed to image the mud volcano, is also generally suitable for surveys of other small seafloor targets, such as gas-hydrate reservoirs, fluid-flow features, and submarine massive-sulfide deposits. An electric bipole antenna is set down by a remotely operated vehicle on the seafloor sequentially in two perpendicular polarizations at each transmission station. Two orthogonal horizontal electric field components are recorded on the seabed by an array of independently deployed nodal receivers (RXs). With two transmitter polarizations, the unique acquisition geometry of the system provides a very rich data set. However, for this geometric setup, conventional marine electromagnetic interpretation schemes (such as normalized magnitude variation with offset plots) have been difficult to implement. We have developed a simple imaging technique, which can be used for a first-step mapping of seafloor apparent resistivity with the GEOMAR system. Images can be produced in just a few minutes on a regular laptop computer, and the robustness of the approach was demonstrated using two synthetic data sets from simple seafloor models. The method was then applied to the real data acquired at the North Alex mud volcano in 2008. Results found increased apparent sediment resistivities of up to 4 Ωm near the center of the mud volcano occurring at source-RX offsets greater than 500 m, which mapped to apparent depths of greater than 150 m. This may be caused by large quantities of free gas or freshwater in the sediment pore space.

INTRODUCTION

Marine mud volcanoes are common features on the seafloor, especially in the Caspian and Mediterranean Seas. They can be found in active and passive margins, where fluid processes at several kilometer depth produce geologic and geochemical effects in the overlying shallow sediments. Often, mud volcanoes are produced by upward migrating fluids that may originate from deeper hydrocarbon reservoirs, and therefore the study of such mud volcanoes is helpful in understanding a petroleum system as a whole. Kopf (2002) provides a good general review of the literature on mud volcanoes in the marine environment, whereas Dupre et al. (2007), Hensen et al. (2007), and Feseker et al. (2009) describe previous work on mud volcanoes in the Mediterranean region. In 2007, the Helmholtz Centre for Ocean Research Kiel (GEOMAR), began a project to study the mud volcanoes in the West Nile Delta (WND); Feseker et al. (2010) give an overview of some early results of the WND project, which are mainly geochemical and geothermometric in nature. In Feseker et al. (2010), fluids rich in hydrocarbons and highly depleted of chloride were recovered at two mud volcanoes: Giza and North Alex. Elevated temperature measurements (in some cases, as high as 70°C at North Alex, 6 m beneath the seafloor) indicate significant activity at both sites; indeed, venting was observed during the GEOMAR research cruises, although the time scale is unknown.

Figure 1a shows an overview map of the WND; the two mud volcanoes of interest to the GEOMAR WND project are indicated by the red stars. The focus of this paper is on the eastern mud vol-

Manuscript received by the Editor 12 January 2014; revised manuscript received 18 October 2014; published online 6 February 2015.
[1]Colorado School of Mines, Department of Geophysics, Golden, Colorado, USA. E-mail: aswidins@mines.edu.
[2]Helmholtz Centre for Ocean Research Kiel (GEOMAR), Geodynamics Department, Kiel, Germany. E-mail: shoelz@geomar.de; mjegen@geomar.de.

cano, North Alex, which is located in close proximity to several gas production fields, and therefore it is a feature of interest to the oil and gas industry. Figure 1b shows a 2D seismic image across the center of North Alex (modified from Hölz et al., 2015). A near-surface gas cap is clearly visible (at a depth of no more than approximately 10 m beneath the seafloor, although in some cases almost reaching the surface) but the seismic image beneath this horizon is highly incoherent due to the lack of underlying reflectors by the active reworking of the sediments, as well as from scattering and attenuation by the overlying low-velocity, gas-saturated zone. Bialas et al. (2010) describe similar incoherence in high-resolution seismic images acquired using a small-scale 3D seismic system. A major geological and geophysical problem is to determine the nature of the fluids lying beneath the gas cap, and the difficulty of interpreting the seismic image motivated the detailed examination of complementary techniques, such as marine electromagnetic surveys.

According to Archie's law (Archie, 1942), if freshwater or gas is present in the pore space, the electric resistivity of the sediment will be increased. A decrease in porosity through, for example, sediment compaction will also increase resistivity. Thus, electromagnetic methods can provide a complementary tool to seismic methods for imaging the internal structure of North Alex. This is because the electric resistivity of a sedimentary rock is mainly controlled by its fluid content, whereas seismic methods primarily image the geologic structure of the subsurface. Constable (2010) gives a good overview of electromagnetic methods in the marine environment for hydrocarbon exploration. One standard technique is to deploy electromagnetic receivers (RXs) on the seabed and tow an electric bipole transmitter (TX) behind a survey vessel that injects a time varying current into the earth and seawater. The recorded electromagnetic fields are functions of the seafloor resistivity structure. This approach is suitable for large-scale targets, such as conventional petroleum reservoirs, but we felt that the relatively small scale of North Alex (which is approximately 1000 m in diameter) would make such a survey difficult to perform (note however that Weitemeyer et al. [2006] successfully use this method to map even smaller scale shallow marine gas hydrates, and therefore the approach would not have been logistically impossible for North Alex). An alternative technique for small-scale targets, as suggested in theory by Edwards (1997) and successfully performed in the field by Schwalenberg et al. (2005) for gas hydrate exploration, is to tow the TX and RXs along the seabed on a single cable. However, instrumentation previously deployed for scientific studies on the mud volcano, such as permanent seismometers and cable-based temperature arrays, made such an approach untenable because of the high likelihood that the electromagnetic survey cable could have been snagged on the man-made infrastructure. The possibility of unmapped carbonate blocks on the seafloor was also a cause for concern (Dupre et al., 2007; Gontharet et al., 2007).

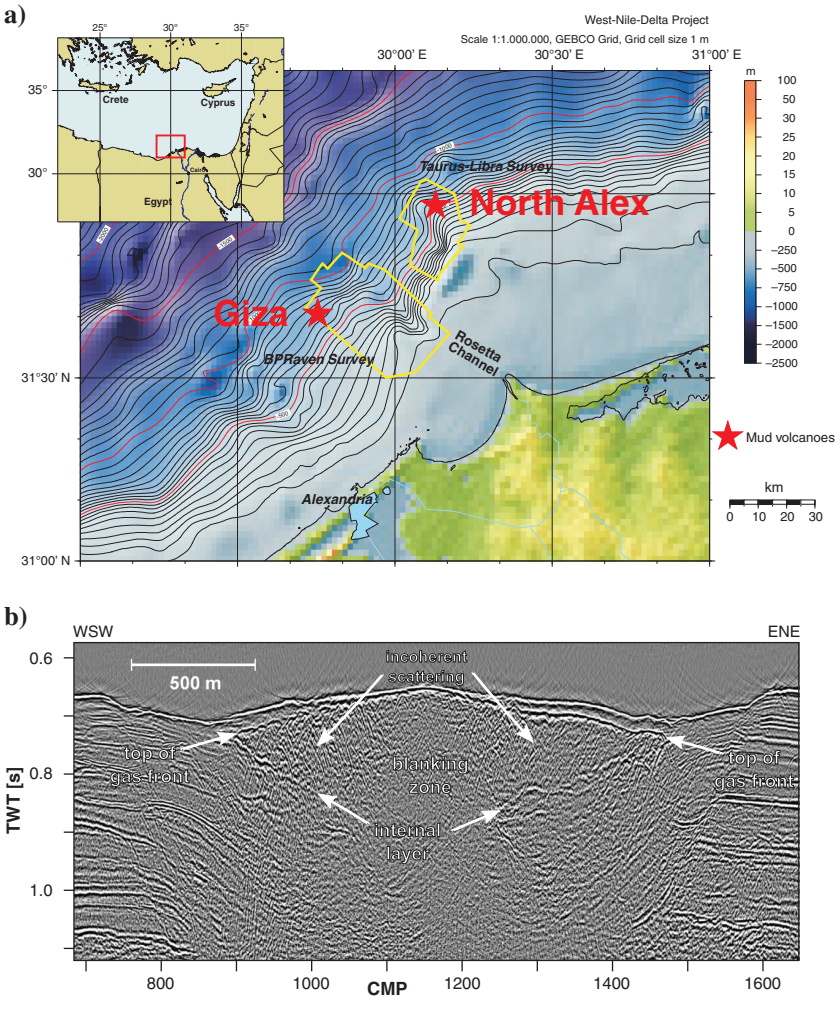

Figure 1. (a) Map of the WND area with mud volcanoes of interest indicated as red stars. Bathymetry from NOAA and (b) seismic image from a 2D line through the center of the North Alex mud volcano, brute stacked, and f-k migrated with a constant velocity of 1500 m/s (modified from Hölz et al., 2015).

In contrast to these two standard techniques, Cairns et al. (1996) attempt an interesting unconventional experiment, where the TX was deployed on the seafloor by the manned submersible *Alvin*, and the electromagnetic fields were measured by standard ocean-bottom RXs. This approach is suitable for surveys of small-scale seafloor targets, such as mud volcanoes, shallow fluid flow features, gas-hydrate reservoirs, and submarine massive sulfide deposits. A modified version of this technique was adapted and modified by the marine electromagnetics group at GEOMAR for the WND project. In a companion paper by Hölz et al. (2015), we describe the experiment and instrumentation in detail. Here, we will summarize some of the most important aspects of the experiment and describe a method to rapidly map seafloor resistivity using this type of system.

Figure 2 shows a sketch of the GEOMAR controlled-source electromagnetic (CSEM) system. A remotely operated vehicle (ROV) places an electric bipole TX stationary on the seafloor in an arbitrary orientation; the 9.1-m-long bipole TX injects a time-varying current of 23.4-A

current as a 50% duty cycle square wave with a period of 4 s. In an ideal experiment, the ROV then lifts the TX off the seafloor, turns 90°, and places it back on the seafloor in an orthogonal direction to the first transmission; the same time-varying current is again injected into the earth and seawater. In practice, a magnetic compass on this ROV allowed the two transmission orientations to be orthogonal to an accuracy of better than 3°.

The RXs, on the other hand, are deployed by free fall from the research vessel and are recovered on the sea surface at the end of the experiment. During the CSEM experiment, these RXs measure two orthogonal components of the horizontal electric field with two sets of silver-silver chloride electrodes separated by a distance of 10 m at a frequency of 10 kHz; this high sampling rate was chosen to properly record early time transient data at short offsets. After stacking, the noise on the transient decay curves approaches 10^{-9} V at 1 s (note that this quantity has not been normalized to the TX moment). The electric bipole arms on the RXs are designed to rest orthogonally on the seafloor, and in the WND experiment, each station was visited by the ROV to ensure this was the case by video inspection. The RXs can also be switched into a magnetotelluric (MT) mode in which natural field variations are recorded at a lower sampling rate of 10 Hz. In addition to the two horizontal electric field components, all three components of the magnetic field are measured with fluxgate magnetometers in this mode. Although MT data were recorded during the WND experiment, in this paper, we focus only on the high-frequency electric field measurements from the CSEM acquisition.

Each TX-RX pair has four electric field measurements: two orthogonal electric field components recorded from each of the two orthogonal bipole transmissions. The nature of the acquisition presents difficulties for conventional interpretation because each TX-RX pair has its own relative rotation and, because of the circular shape of the mud volcano, the instruments were not laid out in a standard survey grid. Similar land based experiments and corresponding interpretation problems are described in Bibby (1977, 1986), Risk et al. (1993), and Caldwell and Bibby (1998), all of whom suggest normalizing the data to a DC half-space current density (which is independent of conductivity) to produce rotationally invariant tensors for easier interpretation. However, their approach is developed specifically for surveys on land. In the marine environment, the DC flow is mainly governed by the conductivity of the seawater, and therefore the data normalization procedure described in the previous set of papers is not as straightforward.

In this paper, we describe an alternative method to rapidly produce apparent resistivity maps of the seafloor using data from a marine system with two TX and RX polarizations from a rotational invariant, which we construct from the measured data. The main purpose of the method is to obtain a first-pass look at the data, in particular to quality control it for acquisition footprints and to determine if any anomalies are present. In principle, our approach is similar to what is used in many other geophysical prospecting applications, such as land-based electric surveys, where pseudosections are produced prior to modeling and inversion to rapidly image the data (see, e.g., Hallof, 1964; Loke and Barker, 1996). Another similar concept is the normalized magnitude versus offset plot (see, e.g., Ellingsrud et al., 2002), which is directly determined from the data and commonly used in commercial marine CSEM to detect anomalous zones in the subsurface before more complicated modeling and inversion. Given the unique nature of the GEOMAR CSEM experiment, a novel theory to properly reduce and map the measured data is required. Our general workflow is to (1) process the raw data, (2) make an apparent resistivity map, (3) invert the data with 1D layered models, and (4) forward model and invert the data in 3D (this is still under development, although Sommer et al. [2013] present some preliminary results on this topic). The marine electromagnetics group at GEOMAR performs this flow on all data sets that are collected. This paper is mainly concerned with step (2), which has required the development and examination of some new theory. In our companion paper by Hölz et al. (2015), we describe and examine step (3) in detail also using the WND data set. In the present paper, we will first describe the fundamental theory of a rapid imaging technique. We then illustrate its application using two synthetic data examples from simple models of shallow resistive targets. Finally, we apply this methodology to the WND, North Alex mud volcano data set. The work described here is an extension of the results presented in Swidinsky et al. (2013).

FUNDAMENTAL THEORY

Figure 3 shows the general geometry of a single TX-RX pair. The distance between the instruments is denoted by r, and at sea it can be determined from standard acoustic positioning data. Note that this figure assumes that the two TX orientations are orthogonal; in Figure 3 in Hölz et al. (2015), we consider the case of nonperpendicular antennas. For the WND experiment, we used an ultrashort baseline transponder system to measure distance with a 0.2% accuracy,

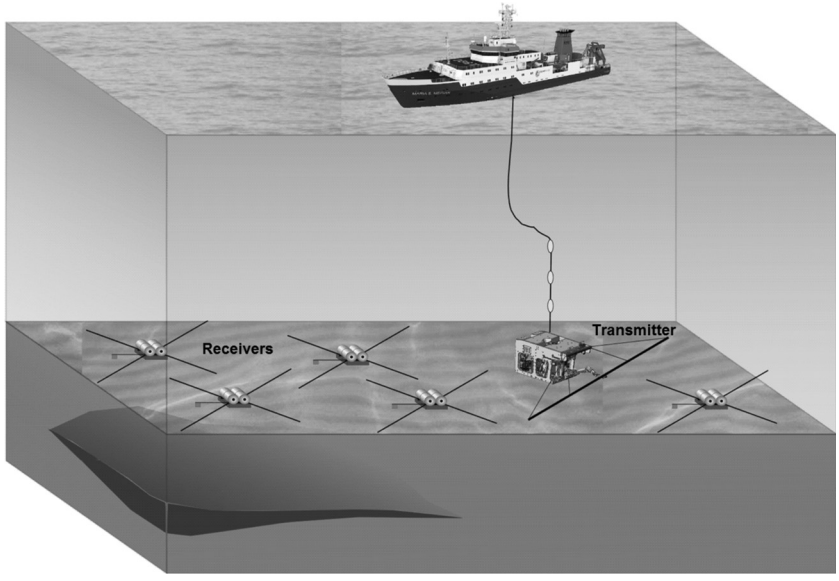

Figure 2. Illustration of the GEOMAR marine CSEM system. The bipole TX is set down by an ROV on the seafloor sequentially in two perpendicular orientations for each transmission station (modified from Sommer et al., 2013).

which is typical for most marine surveys. The system will record a set of transient electric fields E_{11}, E_{12}, E_{21}, and E_{22}, where the first subscript describes the RX orientation, and the second subscript describes the transmission orientation (see Figure 3a). If the TX coordinate system is now rotated clockwise by an angle θ, and the RX coordinate system is rotated clockwise by an angle ϕ (see Figure 3b), we obtain a new set of electric fields $E_{1'1'}$, $E_{1'2'}$, $E_{2'1'}$, and $E_{2'2'}$. Let us assume that there are two orthogonal transmission orientations with equal source moment and two orthogonal electric field measurements. Let us also assume that the TX and RX can be approximated as dipoles (rather than bipoles of finite length). Although Streich and Becken (2010) show the importance of using the complete bipole solution, the dipole approximation is a valid assumption in our case because the 9.1-m-long TX produces the same fields as a point dipole at offsets greater than 50 m (one of the smallest offsets in the WND survey). Under these simplifying conditions, the two sets of electric fields are related by the expression

$$\begin{bmatrix} E_{1'1'} & E_{1'2'} \\ E_{2'1'} & E_{2'2'} \end{bmatrix} = \begin{bmatrix} \cos(\phi) & \sin(\phi) \\ -\sin(\phi) & \cos(\phi) \end{bmatrix} \begin{bmatrix} E_{11} & E_{12} \\ E_{21} & E_{22} \end{bmatrix} \times \begin{bmatrix} \cos(\theta) & \sin(\theta) \\ -\sin(\theta) & \cos(\theta) \end{bmatrix}^T, \quad (1)$$

which has the more compact matrix form

$$\mathbf{E}' = \mathbf{R_{RX}} \mathbf{E} \mathbf{R_{TX}^T}, \quad (2)$$

where $\mathbf{R_{RX}}$ and $\mathbf{R_{TX}}$ denote the matrix containing the rotations of the RX and TX, respectively, whereas $\mathbf{E}'$ and $\mathbf{E}$ correspond to the matrix containing the rotated and unrotated electric fields. Constable and Cox (1996) describe a similar rotation for a single TX polarization with an arbitrary rotation with respect to an RX. In our case, using the following matrix identities,

$$\begin{aligned} \det(\mathbf{AB}) &= \det(\mathbf{A}) \det(\mathbf{B}), \\ \det(\mathbf{A^T}) &= \det(\mathbf{A}), \\ \det(\mathbf{R_{TX}}) &= \det(\mathbf{R_{RX}}) = 1, \end{aligned} \quad (3)$$

where $\mathbf{A}$ and $\mathbf{B}$ are arbitrary matrices, we can take the determinant of both sides of equation 1 to write

$$\det\left(\begin{bmatrix} E_{1'1'} & E_{1'2'} \\ E_{2'1'} & E_{2'2'} \end{bmatrix}\right) = \det\left(\begin{bmatrix} E_{11} & E_{12} \\ E_{21} & E_{22} \end{bmatrix}\right). \quad (4)$$

Therefore, the determinant of the matrix containing the set of four electric field measurements is invariant with respect to the rotation of TX or RX, and, consequently, is also independent of the overall choice of the coordinate system. Using this result, we can define an electric field invariant $E_{\text{invariant}}$ for each TX-RX pair, using the set of four electric field measurements as

$$E_{\text{invariant}} = \det\left(\begin{bmatrix} E_{11} & E_{12} \\ E_{21} & E_{22} \end{bmatrix}\right). \quad (5)$$

By constructing this invariant from the electric field components recorded during a survey, the data set is simplified by removing the relative rotation of each TX and RX pair and the only remaining geometric factor is the TX-RX offset. In Hölz et al. (2015), we more rigorously examine a variety of rotational invariants, all of which can be used to interpret data from an electromagnetic survey with two TX polarizations that are not necessarily perpendicular. Indeed, under the assumptions of two perpendicular TX antennas with equal source moment, our invariant given in equation 5 is identical to the first invariant I1 described in this companion paper. For the purpose of the present paper, we will only make use of this first invariant as a first step to image our data (although it is possible that a similar method can be applied on the other invariants). Furthermore, Hölz et al. (2015) examine the situation where the transmission directions are nonperpendicular (although their orientations are still well known); in the case of the WND, however, almost all stations were very close to orthogonal due to the highly maneuverable ROV carrying a magnetic compass (all orientation information is logged during the course of the experiment), and therefore the simplifying assumptions contained in equation 1 are valid for our data set.

From Maxwell's equations, the basic differential equation for time-varying electromagnetic fields in conductive media is the diffusion equation, which can be written in general for an electric field measurement E in a whole-space of conductivity σ and magnetic permeability μ as

$$\nabla^2 E = \mu\sigma \frac{\partial E}{\partial t}. \quad (6)$$

From dimensional analysis of equation 6, we can write

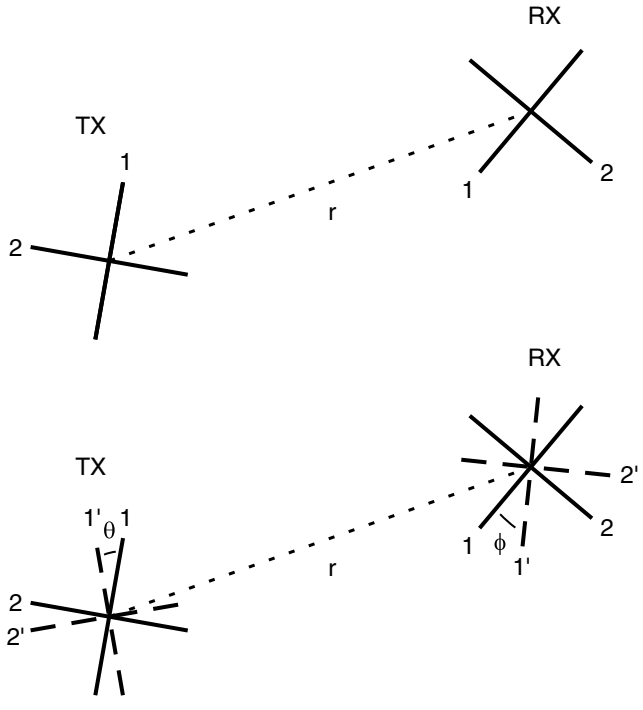

Figure 3. Schematic of TX and RX dipole geometries. The offset between the TX and RX is denoted by r, and the rotation of the TX and of RX with respect to their original orientation is denoted by θ and ϕ, respectively.

$$\frac{1}{[\text{lengthscale}]^2} = \frac{\mu\sigma}{[\text{timescale}]}. \quad (7)$$

This expression can be converted into an equation for the characteristic time τ of the field as

$$\tau = \frac{\mu\sigma r^2}{s}, \quad (8)$$

where r is the TX-RX offset and s is a scaling constant, which reflects the nonexact derivation of equation 8. Ward and Hohmann (1988) derive equation 8 analytically for an impulsive plane-wave source in a whole-space, and show that in this case, the scaling constant s in this case is equal to six. In Appendix A, we extend this result and analytically derive equation 8 for an infinitesimal electric dipole source in a whole-space. In this situation, there are a range of geometries to consider and s can vary between six and 16. In general, given that the fields produced by a finite source can be constructed from elementary plane-wave solutions, one may deduce that equation 8 must be valid for all such sources but will have a modified value of s to reflect variations in geometry and dimensionality.

It is typical in a time-domain electromagnetic prospecting system to switch on (or switch off) the TX abruptly, so that the measured electric field is the step response of the system. The recorded step response can be converted into the impulse response by taking the derivative of the data with respect to time (or by deconvolving the TX current waveform from the RX measurement). Alternatively, we can take the derivative of the data with respect to *logarithmic time* as suggested in Edwards (1997). This is a simple approach that conforms to the log-based time scales often used in time-domain electromagnetics, and we shall refer to the newly derived measurement as the *pseudoimpulse response*. This pseudoimpulse response can be derived from any step-on (or step-off) electric field measurement; in Appendix A, we examine the case of inline, broadside, and invariant electric fields in a whole-space. If we treat the arrival time τ as the peak arrival time of the invariant pseudoimpulse response (as we will in this paper), the value s in equation 8 can be determined analytically for certain simple cases. Appendix A shows that s is equal to approximately 6.3 for the invariant pseudoimpulse response in a homogeneous, isotropic whole-space. For more complicated models, s can be determined numerically. For a simple double half-space model, Appendix B shows that s is approximately equal to four for most values of seafloor conductivity. Equation 8 can be rearranged to obtain an expression for the arrival time apparent resistivity ρ_a given as

$$\rho_a = \frac{\mu r^2}{s\tau}. \quad (9)$$

Under the assumption of a double half-space (corresponding to $s = 4$), an apparent resistivity can be calculated for each TX-RX pair directly from the data (i.e., from the TX-RX offset and the peak arrival time of the invariant). If the seafloor is uniform within the scale of the experiment, this apparent resistivity will be equal to the actual resistivity. However, if the seafloor conductivity structure is more complex, the apparent resistivity will only be an approximation of the true resistivity.

TWO SYNTHETIC EXAMPLES

Figure 4a shows three basic seafloor models to illustrate the use of the invariant pseudoimpulse arrival time, whereas Figure 4b shows the corresponding apparent resistivity sections. The seawater has a conductivity of 0.33 Ωm and a depth of 1000 m. The first model (model 1) is a homogeneous seafloor with a resistivity of 1 Ωm. The other two models (models 2 and 3) include a 100-m-thick resistive zone buried at a depth of 50 m. The resistivities and depth scales are representative of a shallow gas-filled target in high-porosity marine sediment. Figure 4c shows the invariant step-on response for the three 1D layered models at an offset of 200 m, calculated using the 1D algorithm described in Edwards (1997) for the inline and broadside fields (for a 1D model, the invariant is a product of these two quantities). Note that the unit of the invariant is V^2/A^2m^4, as it derived from the product of source normalized electric field measurements. As expected from a field that obeys the electromagnetic diffusion equation, the bulk arrival of the field comes at an earlier time for a more resistive subsurface zone. Figure 4d shows the normalized derivative of the step response with respect to logarithmic time (the invariant pseudoimpulse response). The invariant pseudoimpulse arrival time τ can be seen as a clear peak and is a function of the subsurface resistivity. There are three different values of the arrival time τ for the three different models. We shall use these peak arrival times to calculate apparent resistivity curves through equation 9. Figure 4b shows the apparent resistivity plotted against the TX-RX offset, derived from the arrival time over a range of offsets. The apparent resistivity of the homogeneous seafloor is identical to the original model, which is expected because the theory was developed with the assumption of a double half-space and that the scaling constant $s = 4$. The apparent resistivity of the resistive zone models first increases with offset, before starting to decrease again at larger offsets. In all cases, the apparent resistivity is less than the true resistivity, and it is spread out over a large range of offsets. This is consistent with apparent resistivity curves produced from DC resistivity methods or conventional electromagnetic soundings. Hölz et al. (2015) examine the invariant sensitivity compared with the pure inline and broadside modes. Results show that the invariant sensitivity is comparable with the inline sensitivity. However, this sensitivity analysis is more suitable for an inversion study, which is the topic of our companion paper.

As a second synthetic example, we choose a simple 3D seafloor model with dimensions and resistivities again comparable with shallow, gas-filled sediment (Figure 5a). For simplicity, electric fields are calculated along a line through the center of the model using the thin sheet code described in Swidinsky and Edwards (2010). Each TX-RX pair still has four electric field measurements: two orthogonal electric field components recorded from each of the two orthogonal bipole transmissions. The profile is 2000 m long, and the station spacing is 50 m for the TX and the RXs (the stations shown in the figure are for illustration only). The model consists of a double half-space with 0.33 Ωm seawater and a 1-Ωm uniform seafloor containing a 50-m-thick, 500-m-wide, 10-Ωm resistive sheet buried at a depth of 75 m. Figure 5b (left) shows an example of the rotational invariants after switch-on for two different TX-RX pairs (shown in red and blue). Again, we can create the invariant pseudoimpulse response by taking the derivative of the invariant step-on response with respect to logarithmic time (Figure 5b, right). It is the arrival times of these invariant pseudoimpulse responses

that are used to calculate apparent resistivities. Figure 5c shows an arrival time apparent resistivity pseudosection of the simple 3D model, produced in the same way as the classic DC resistivity pseudosection — but with arrival time apparent resistivities plotted at the midpoint between the TX and the RX as illustrated by the white dots on the pseudosection. The offset scale is related to depth in that larger offsets have greater depths of penetration. As in the previous example, the scaling constant $s = 4$; this produces an apparent resistivity equal to the true resistivity when data are recorded over the double half-space host. However, over the resistive target, the pseudosection clearly indicates a resistivity anomaly, but this anomaly is significantly different from the target in the original model: The lateral boundaries of the target are well defined, but the depth and thickness are poorly imaged (in a manner similar to in the previous example). Nonetheless, the purpose of our approach is to rapidly assess if and where an anomaly may occur before proceeding to higher level interpretation methods. One notable feature on the sections is the "pant-leg" artifact often observed on DC resistivity or electromagnetic pseudosections for similar finite-sized targets. The pant legs can be understood by first considering a situation in which the TX and RX symmetrically straddle the resistive target. As the offset increases to the point at which the instruments are both far away from the opposite edges of the sheet, the electromagnetic fields and corresponding apparent resistivities are not strongly affected by the presence of the resistor (although it lies between them). In contrast, if the TX or RX lies in a fixed position above the resistive target, even as the offset increases, the fields must always pass through the resistive zone. Thus, the apparent resistivity at these corresponding pseudosection midpoints increases downward and outward, whereas the apparent resistivity directly beneath the target decreases downward to produce the two distinct pant legs.

APPLICATION TO THE WEST NILE DELTA

Figure 6a shows a high-resolution bathymetric map of the North Alex mud volcano. The GEOMAR CSEM survey geometry is overlain on the volcano; the black crosses indicate the ROV deployed TX positions, whereas the white boxes indicate the RX stations. The

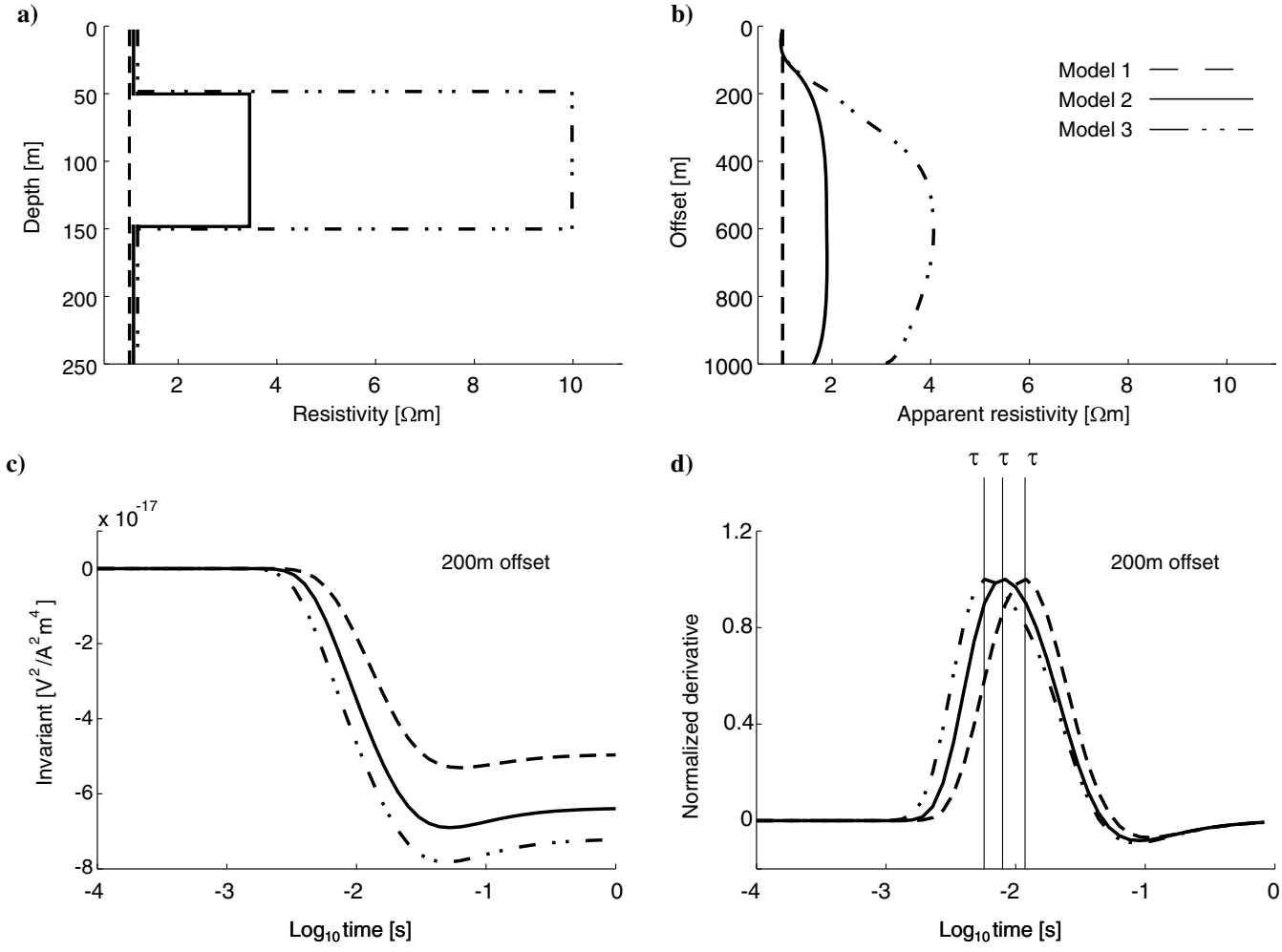

Figure 4. (a) Three simple layered earth seafloor models. The sea has a depth of 1000 m and a resistivity of 0.33 Ωm, (b) apparent resistivity versus offset profiles for the three models, (c) step-on rotational invariants for the three models at an offset of 200 m, and (d) amplitude normalized pseudoimpulse responses of the rotational invariant for the three models at an offset of 200 m. The arrival times τ are indicated by the vertical lines.

water depth and maximum TX-RX offsets are approximately 500 and 1000 m, respectively.

Figure 7 shows the invariants' step-on responses calculated, using equation 5, from the data measured during the GEOMAR CSEM survey for all 462 TX-RX pairs. Because the TX-RX offsets range from less than 50 m to more than 500 m, the data must be reduced in two ways for a proper comparison. First, because the amplitudes vary as a function of $1/r^6$ (the power law of a dipole squared), each invariant is normalized by its late time, DC value. Second, because the bulk arrival time of the invariants varies as

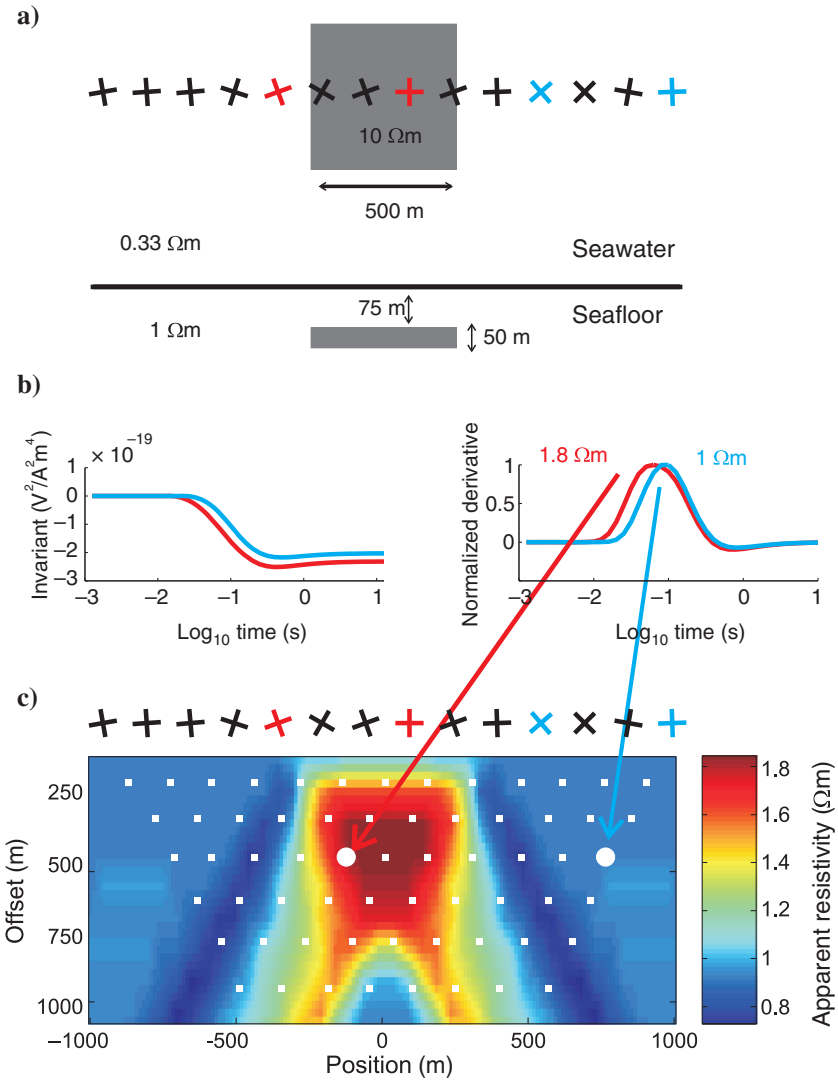

Figure 5. (a) Simple 3D model (plan and section view). The crosses on the model plan view can represent the TXs or RXs. The rotations are arbitrary and for illustration only; they are eliminated by the calculation of the invariant. (b, left) Step-on rotational invariants curves (in red and blue) corresponding to the red and blue station pairs shown in the model sketch and (b, right) amplitude normalized pseudoimpulse responses of the rotational invariant for the two station pairs. (c) Apparent resistivity pseudosection calculated from the arrival times of the invariant derivative. The white dots schematically indicate the apparent resistivity plotting points, midway between each TX and RX at a depth equal to their offset. Note that our convention is to make red resistive and blue conductive.

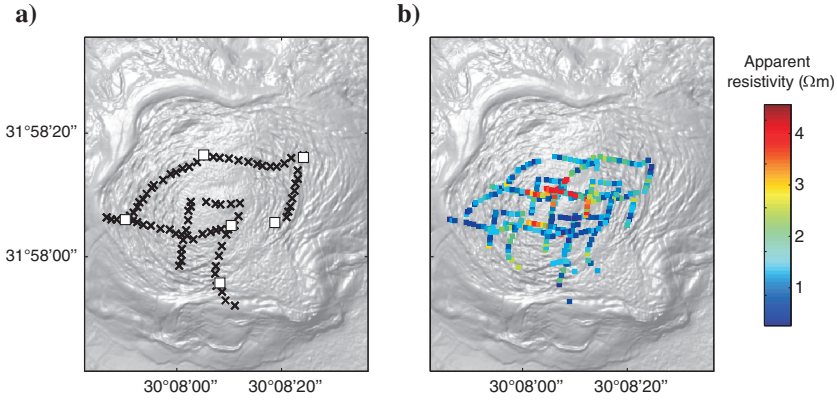

Figure 6. (a) Autonomous underwater vehicle (AUV) based microbathymetric map of the mud volcano with TX (crosses) and RX (white boxes) stations and (b) apparent resistivity plotted at the midpoint of each TX-RX pair using the data shown in Figure 8. The number of apparent resistivity points (462) is equal to the product of the number of TX stations (77) times the number of RX stations (6). Bathymetry from Feseker et al. (2010), originally provided courtesy of BP.

a function of r^2 (as can be seen in equation 9), the time axis is normalized to the characteristic time of seawater $\tau_0 = \mu\sigma_0 r^2$ (similar to the plots in Cheesman et al., 1987), where σ_0 is the conductivity of seawater. During the experiment, the seawater conductivity was measured continuously with a conductivity-temperature-depth (CTD) probe, but note that the choice of the normalization conductivity is arbitrary because our primary purpose is to remove the r^2 variation. The resulting reduced invariants can be readily compared for all of the TX-RX pairs; the real data are qualitatively consistent with the theoretical curves shown in Figures 4 and 5, and for reference, the dashed gray curve in Figure 7 shows the invariant response of a double half-space with a 1 S/m (1 Ωm) seafloor and 3 S/m (0.33 Ωm) seawater. Real data recorded before a dimensionless time of −2 are just noise, whereas after this time, there is significant variability in the shape and arrival of the signal. This implies a variable resistivity of the subsurface, but it may also be due to the effect of additional factors, such as variable water resistivity and finite water depth. Figure 8 shows common offset bins of the invariant pseudoimpulse responses calculated from the 462 curves shown in Figure 7. The responses have been normalized to a peak amplitude, but the time scale is now a real time (unlike the normalized time scale in Figure 7). We muted the early times on these "traces" because noise

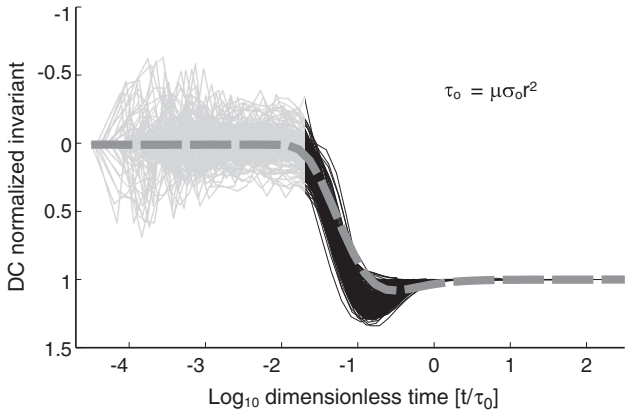

Figure 7. Step-on invariants from the mud volcano experiment for all 462 TX-RX pairs (black curves). The data have been normalized by the late time, static response and with a dimensionless time. These two normalizations allow multioffset data to be compared on the same scale. The dashed gray curve corresponds to the modeled invariant for a double half-space with a 1 S/m (1 Ωm) seafloor and 3 S/m (0.33 Ωm) seawater.

in the early time invariant step response (from data recorded before a dimensionless time of –2) results in very noisy derivatives. For reference, the dashed gray curves in Figure 8 show the normalized invariant pseudoimpulse response of a double half-space with a 1 S/m (1 Ωm) seafloor and 3 S/m (0.33 Ωm) seawater. The arrival times of the invariant pseudoimpulse responses increase with offset in a classic r^2 behavior, but the variability of the real data within each offset bin may be attributed to variations in seafloor resistivity (but also to variations in offset when the TX-RX separation is small). The arrival time of each of these pseudoimpulse responses is used to calculate the apparent resistivity via equation 9. In general, once the arrival times are picked (either manually or automatically), the conversion to apparent resistivity using equation 9 is practically instantaneous; taking into account all of the required steps (creating invariants, converting to pseudoimpulse responses, picking arrival times, and converting to apparent resistivity), the procedure takes no more than a few minutes on a regular laptop.

Figure 6b shows the apparent resistivity map derived directly from the arrival times of the invariant pseudoimpulse responses. Apparent resistivities are plotted at the midpoint between each TX-RX pair and range from less than 1 Ωm around the sides of the mud volcano to as much as 4 Ωm near the center. Note that we are unfortunately unable to produce a pseudosection like Figure 5c because the data density and 3D geometry of the experiment are not suitable for such an imaging procedure. However, Figure 9 shows apparent resistivity slices corresponding to the six different offset bins in Figure 8 for the WND experiment. Offsets over 500 m show significantly increased apparent resistivities, which may correspond to free gas or freshwater in the deeper sediments within the mud volcano. These resistivities are located near the middle of the mud volcano; this may be a real geologic effect but may also be due to the geometry of the experiment because the survey was designed to have the largest TX-RX offsets centered near the middle of the mud volcano. Regardless, the presence of a deeper resistive zone is directly evident in the data. Sommer et al. (2013) investigate the effect of bathymetry on the electromagnetic data at North Alex and find that only small offsets (<125 m) are affected by seafloor topography (typically varying by no more than 20 m across the mud volcano with small scale depressions of up to 3 m depth); this implies that the apparent resistivity anomaly is not a bathymetric effect, but it is produced by a real subsurface structure. In Appendix B, we show that for offsets greater than approximately 700 m, the finite water depth of 500 m will result in decreased apparent resistivity estimates, and therefore the apparent resistivity image at the center of the volcano at large offsets may actually

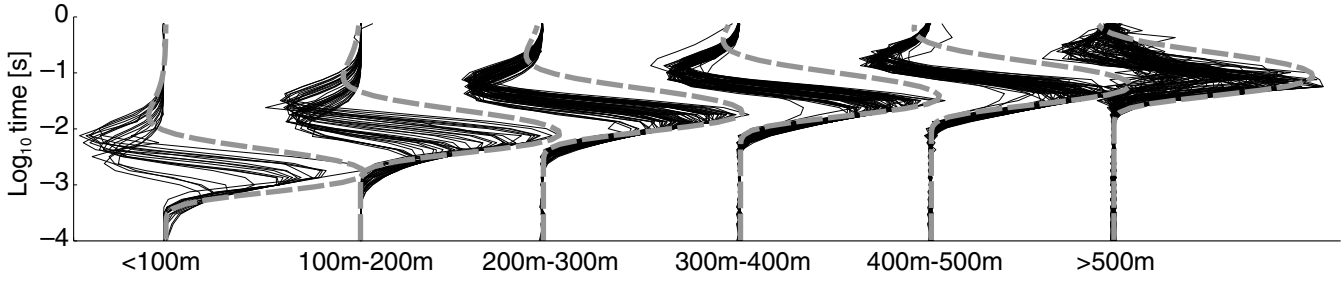

Figure 8. Normalized invariant pseudoimpulse responses from the WND mud volcano experiment for all 462 TX-RX pairs (black curves). The transients are sorted into common offset bins to demonstrate the quality of the data and its consistency with the theory. A mute has been applied to enhance the arrival times and remove early time noise. The dashed gray curve corresponds to the modeled invariant pseudoimpulse response (normalized) for a double half-space with a 1 S/m (1 Ωm) seafloor and 3 S/m (0.33 Ωm) seawater.

be underestimated. More generally, from equation 9, if the scaling constant s is incorrectly chosen to be too high, the apparent resistivity will be underestimated and vice versa.

DISCUSSION

The increased apparent resistivities from larger offset data acquired at the North Alex mud volcano in the WND suggest the presence of freshwater or free gas in the sediment pore space well beneath the gas cap, which itself is no more than 10 m beneath the seafloor as indicated in Figure 1. The increase in resistivity is in contrast to the observation by O'Suilleabhain et al. (2012), who find decreased resistivities within a suspected ancient, buried mud volcano offshore Malaysia. This latter effect may be due to vertical upward movement of warm saline pore water. Based on the evidence, we believe that if similar warm water movement occurs at North Alex (and indeed, Feseker et al. [2010] observe high surface temperatures at the center of the mud volcano), the fluid must be very fresh (in contrast to the pore water in the surrounding sediments), and/or it must contain significant quantities of free gas to produce the increased resistivities that we observe; in support of this conclusion, Feseker et al. (2010) also show evidence of desalinization in the pore water from geochemical data. It is interesting to note that no increased apparent resistivities are observed for short offsets, as would be expected if the gas cap (only a few tens of meters beneath the seafloor) was highly saturated. Therefore, the electromagnetic data suggest that the gas saturation is not high enough to change the apparent resistivity (although an exact saturation value cannot be determined from the apparent resistivity, which is only a qualitative estimate). Such a conclusion cannot

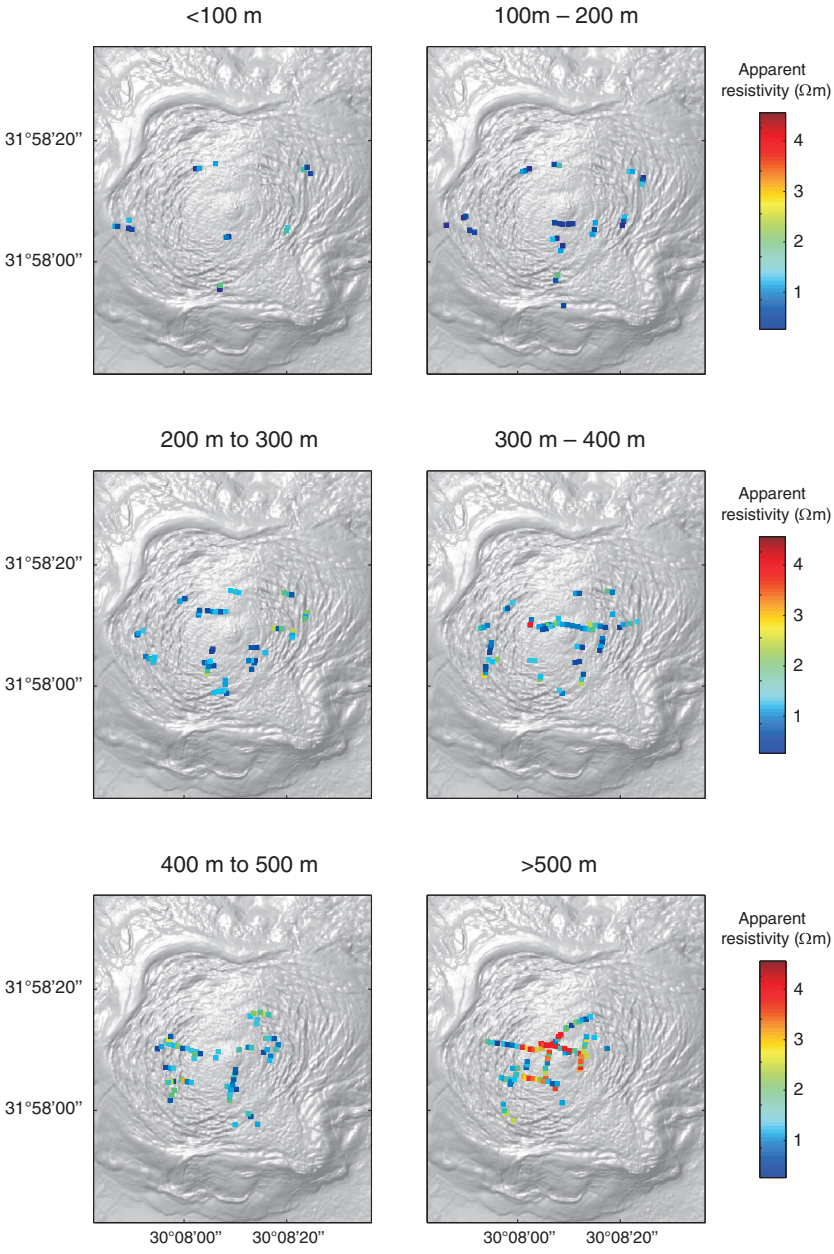

Figure 9. Apparent resistivity map sorted into common offset bins. Higher resistivities correspond to offsets greater than 500 m and therefore to deeper portions of the mud volcano. Note that our convention is to make red resistive and blue conductive.

be reached with the seismic data alone because a small amount of gas decreased the P-wave velocity in a similar manner to a large amount of gas; a good example of this effect is demonstrated in Domenico (1977). Figure 4 suggests that the conversion from offset to depth is approximately 3:1 when using the arrival times of the invariants to produce apparent resistivity pseudosections. Given that increased apparent resistivities are only observed at offsets between 500 and 1000 m, this implies that any high concentrations of gas or freshwater occur more than approximately 150 m beneath the seafloor, deep within the mud volcano and the corresponding zone of seismic incoherence. However, because the apparent resistivities are imaged only as a function of offset (and corresponding pseudodepth), this conclusion is not a particularly strong one; a true inversion must be preformed to more properly understand the distribution of resistivity with depth. In Hölz et al. (2015), we perform such an inversion and find increased resistivities with depth, in general agreement with the qualitative estimates made in this paper; we also evaluate the connection more quantitatively between resistivity and fluid content in the deep and shallow sections of the mud volcano. This more quantitative approach also allows us to eliminate the possibility of resistivity increase by compaction related porosity reduction using a simple application of Archie's law for typical shallow sediments.

CONCLUSIONS

In 2008, GEOMAR conducted a survey of a mud volcano in the WND as a proof-of-principle test of a novel marine CSEM experiment suitable for small ($\sim$1 km^2) seafloor targets. Such an approach requires unique instrumentation and interpretation methods. In this paper, we describe novel methodology to produce apparent resistivity maps of the mud volcano, which can be used to rapidly quality control data and create anomaly maps for first-pass imaging studies. Increased apparent resistivities of up to 4 Ωm are evident at the center of the volcano, possibly caused by the presence of freshwater or free gas. These increased resistivities are in contrast to observations in other parts of the world, suggesting that the fluid characteristics of mud volcanoes can be quite variable.

The apparent resistivity mapping approach that we describe here is only the first step of a multistage interpretation process for data collected using a marine CSEM system with two TX polarizations. Invariants can next be inverted for layered 1D models or even for 2D or 3D models using fast and efficient graphics processing unit (GPU) parallelized time-domain forward codes. Without these more advanced techniques, a geologic interpretation is rather limited. However, rapid imaging of the seafloor using an arrival time apparent resistivity is an approach that can be used to quickly establish the presence of resistivity anomalies (or even simply to quality control the data), before higher level interpretation methods are applied. Our data reduction and imaging approach are not particularly suitable for conventional marine CSEM with a towed TX operating in the frequency domain. However, the time-domain, two-polarization, stationary TX survey is an alternative electromagnetic technique that can be applied to a variety of small-scale targets such as mud volcanoes, gas hydrate deposits, shallow gas features, or even marine mineral deposits. Therefore, our reduction and imaging approach may be of value if measurements similar to the WND data set are acquired in the future for these applications.

ACKNOWLEDGMENTS

We kindly thank RWE Dea AG (Hamburg, Germany) for campaign funding, and RWE Dea's Egypt branch as well as their concession partner BP (operator) for helpful collaboration, assistance in permissions, and organizational matters. Bathymetric data were originally provided courtesy of BP. We would also like to thank associate editor R. Mittet as well as J. I. Nordskag and two anonymous reviewers for their helpful comments.

APPENDIX A

ARRIVAL TIMES IN A WHOLE-SPACE

The inline field

Consider an electric dipole carrying a current I and having a length dl buried in a whole-space of conductivity σ and magnetic permeability μ. The inline step-on response of the electric field $E^{\text{step}}_{\text{inline}}$, a distance r from the dipole, measured at a time t after the current is switched on can be found in equation 2.50 of Ward and Hohmann (1988) as

$$E^{\text{step}}_{\text{inline}} = \frac{Idl}{4\pi\sigma r^3}\left[\frac{4}{\sqrt{\pi}}\theta r e^{-\theta^2 r^2} + 2erfc(\theta r)\right], \tag{A-1}$$

where $\theta = \sqrt{\mu\sigma/4\ t}$. We can obtain the inline impulse response $E^{\text{impulse}}_{\text{inline}}$ of the electric field by taking the time derivative of the step response as

$$E^{\text{impulse}}_{\text{inline}} = \frac{\partial E^{\text{step}}_{\text{inline}}}{\partial t} = \frac{Idl}{4\pi\sigma r^3}\left[\frac{4}{\sqrt{\pi}t}\theta^3 r^3 e^{-\theta^2 r^2}\right]. \tag{A-2}$$

Defining the *pseudoimpulse* response $E^{\text{pseudoimpulse}}_{\text{inline}}$ as the derivative of the step response with respect to logarithmic time following Edwards (1997), we may then write

$$E^{\text{pseudoimpulse}}_{\text{inline}} = \frac{\partial E^{\text{step}}_{\text{inline}}}{\partial \log_{10} t} = 2.302 \times t\frac{\partial E^{\text{step}}_{\text{inline}}}{\partial t}. \tag{A-3}$$

The peak arrival time τ of the inline impulse response occurs when the time derivative of A-2 is equal to zero. Carrying out the differentiation, we obtain

$$\frac{\partial E^{\text{impulse}}_{\text{inline}}}{\partial t} = \frac{Idl}{4\pi\sigma r^3}\left[\frac{(\mu\sigma r^2 - 10\ t)}{\sqrt{\pi}t^3}\theta^3 r^3 e^{-\theta^2 r^2}\right]. \tag{A-4}$$

Equation A-4 is equal to zero when $\mu\sigma r^2 - 10\tau = 0$, or when $\tau = \frac{\mu\sigma r^2}{10}$. Therefore, the value of s in equation 8 in this case is 10. Likewise, the peak arrival time of the inline pseudoimpulse response occurs when the time derivative of A-3 is equal to zero. Carrying out the differentiation, we obtain

$$\frac{\partial E^{\text{pseudoimpulse}}_{\text{inline}}}{\partial t} = 2.302 \times \frac{Idl}{4\pi\sigma r^3}\left[\frac{(\mu\sigma r^2 - 6\ t)}{\sqrt{\pi}t^3}\theta^3 r^3 e^{-\theta^2 r^2}\right]. \tag{A-5}$$

Equation A-5 is equal to zero when $\mu\sigma r^2 - 6\tau = 0$, or when $\tau = \frac{\mu\sigma r^2}{6}$, and therefore the value of s in this case is six.

The broadside field

A similar analysis can be carried out for the electric field measured broadside to a grounded electric dipole. The broadside step-on response $E^{\text{step}}_{\text{broadside}}$ can be found in equation 2.50 of Ward and Hohmann (1988) as

$$E^{\text{step}}_{\text{broadside}} = -\frac{Idl}{4\pi\sigma r^3}\left[\left\{\frac{4}{\sqrt{\pi}}\theta^3 r^3 + \frac{2}{\sqrt{\pi}}\theta r\right\}e^{-\theta^2 r^2} + \text{erfc}(\theta r)\right]. \tag{A-6}$$

The broadside impulse response $E^{\text{impulse}}_{\text{broadside}}$ is

$$E^{\text{impulse}}_{\text{broadside}} = \frac{\partial E^{\text{step}}_{\text{broadside}}}{\partial t} = -\frac{Idl}{4\pi\sigma r^3}\left[\frac{(\mu\sigma r^2 - 4\ t)}{\sqrt{\pi}t^2}\theta^3 r^3 e^{-\theta^2 r^2}\right]. \tag{A-7}$$

Similarly, the broadside pseudoimpulse response $E^{\text{pseudoimpulse}}_{\text{broadside}}$ is

$$E^{\text{pseudoimpulse}}_{\text{broadside}} = \frac{\partial E^{\text{step}}_{\text{broadside}}}{\partial \log_{10} t} = 2.302 \times t\frac{\partial E^{\text{step}}_{\text{broadside}}}{\partial t}. \tag{A-8}$$

The peak arrival time of the broadside impulse response occurs when the time derivative of A-7 is equal to zero. Carrying out the differentiation, we obtain

$$\frac{\partial E^{\text{impulse}}_{\text{broadside}}}{\partial t} = -\frac{Idl}{4\pi\sigma r^3}\left[\frac{(\mu^2\sigma^2 r^4 - 18\mu\sigma r^2 t + 40\ t^2)}{4\sqrt{\pi}t^4}\theta^3 r^3 e^{-\theta^2 r^2}\right]. \tag{A-9}$$

Equation A-9 is equal to zero when $\mu^2\sigma^2 r^4 - 18\mu\sigma r^2\tau + 40\tau^2 = 0$, or when $\tau = (\mu\sigma r^2/9 - \sqrt{41})$ or $\tau = (\mu\sigma r^2/9 + \sqrt{41})$. The existence of two roots for equation A-9 indicates the existence of two extrema; this observation can be confirmed by plotting the broadside impulse response as a function of time, which shows that the global maximum is the earlier of the two extrema, and therefore the value of s in this case is $9 + \sqrt{41}$. Similarly, the peak arrival time of the broadside pseudoimpulse response occurs when the time derivative of A-8 is equal to zero. Carrying out the differentiation, we obtain

$$\frac{\partial E^{\text{pseudoimpulse}}_{\text{broadside}}}{\partial t} = -2.302 \times \frac{Idl}{4\pi\sigma r^3} \times \left[\frac{(\mu^2\sigma^2 r^4 - 14\mu\sigma r^2 t + 24\ t^2)}{4\sqrt{\pi}t^4}\theta^3 r^3 e^{-\theta^2 r^2}\right]. \tag{A-10}$$

Equation A-10 is equal to zero when $\mu^2\sigma^2 r^4 - 14\mu\sigma r^2\tau + 24\tau^2 = 0$, or when $\tau = (\mu\sigma r^2/2)$ or $\tau = (\mu\sigma r^2/12)$. Again, two extrema exist for the broadside pseudoimpulse response and the global maximum is the earlier of the two; the value of s in this case is therefore 12.

The invariant field

For a 1D earth, the invariant step-on response $E^{\text{step}}_{\text{invariant}}$ is the product of the inline and broadside fields; in the case of a whole-space, it is the product of equations A-1 and A-6, and is given as

$$E^{\text{step}}_{\text{invariant}} = -\left[\frac{I^2 dl^2}{16\pi^2\sigma^2 r^6}\right] \times \left[\frac{4}{\sqrt{\pi}}\theta r e^{-\theta^2 r^2} + 2erfc(\theta r)\right] \times \left[\left\{\frac{4}{\sqrt{\pi}}\theta^3 r^3 + \frac{2}{\sqrt{\pi}}\theta r\right\}e^{-\theta^2 r^2} + \text{erfc}(\theta r)\right]. \tag{A-11}$$

The invariant impulse response $E^{\text{impulse}}_{\text{invariant}}$ is

$$E^{\text{impulse}}_{\text{invariant}} = \frac{\partial E^{\text{step}}_{\text{invariant}}}{\partial t} = -\left[\frac{I^2 dl^2}{16\pi^2\sigma^2 r^6}\right] \times \left[\frac{4}{\pi t^2}\theta^3 r^3 e^{-2\theta^2 r^2}\right] \times \left[2\theta r(\mu\sigma r^2 - t) + \frac{\sqrt{\pi}}{2}e^{\theta^2 r^2}(\mu\sigma r^2 - 2\ t)\text{erfc}(\theta r)\right]. \tag{A-12}$$

Similarly, the invariant pseudoimpulse response $E^{\text{pseudoimpulse}}_{\text{invariant}}$ is

$$E^{\text{pseudoimpulse}}_{\text{invariant}} = \frac{\partial E^{\text{step}}_{\text{invariant}}}{\partial \log_{10} t} = 2.302 \times t\frac{\partial E^{\text{step}}_{\text{invariant}}}{\partial t}. \tag{A-13}$$

The peak arrival time of the invariant impulse response occurs when the time derivative of A-12 is equal to zero. Carrying out the differentiation, we obtain

$$\frac{\partial E^{\text{impulse}}_{\text{invariant}}}{\partial t} = -\left[\frac{I^2 dl^2}{16\pi^2\sigma^2 r^6}\right] \times \left[\frac{2}{\pi t^4}\theta^2 r^2 e^{-2\theta^2 r^2}\right] \times \left[\sqrt{\pi}\theta r e^{\theta^2 r^2}((1/4)\mu^2\sigma^2 r^4 - 4\mu\sigma r^2 t + 5\ t^2)erfc(\theta r) + 2\theta^2 r^2(\mu^2\sigma^2 r^4 - (17/2)\mu\sigma r^2 t + 5\ t^2)\right]. \tag{A-14}$$

Substituting $s = (\mu\sigma r^2/t)$ into equation A-14 and factoring out a t^2 term, we can obtain a value for s for the invariant impulse response by solving the equation

$$\left[\sqrt{\pi}\sqrt{s/4}e^{s/4}((1/4)s^2 - 4\ s + 5)\text{erfc}(\sqrt{s/4}) + (s/2)(s^2 - (17/2)s + 5)\right] = 0. \tag{A-15}$$

Expression A-15 is unfortunately not easily solved analytically, but a solution can be determined by numerical or graphical techniques. There are two roots for equation A-15 at $s \approx 0.9$ and $s \approx 8.2$. These correspond to two extrema in the invariant impulse response. The global maximum corresponds to the earlier of the two extrema, and therefore $s \approx 8.2$ for the arrival time of the invariant impulse response. Similarly, the peak arrival time of the invariant pseudoimpulse response occurs when the time derivative of A-13 is equal to zero. Carrying out the differentiation, we obtain

$$\frac{\partial E^{\text{pseudoimpulse}}_{\text{invariant}}}{\partial t} = -\left[\frac{I^2 dl^2}{16\pi^2\sigma^2 r^6}\right] \times \left[\frac{2}{\pi t^3}\theta^2 r^2 e^{-2\theta^2 r^2}\right] \times \left[\sqrt{\pi}\theta r e^{\theta^2 r^2}((1/4)\mu^2\sigma^2 r^4 - 3\mu\sigma r^2 t + 3\ t^2)\text{erfc}(\theta r) + 2\theta^2 r^2(\mu^2\sigma^2 r^4 - (13/2)\mu\sigma r^2 t + 5\ t^2)\right]. \quad \text{(A-16)}$$

Again, substituting $s = (\mu\sigma r^2/t)$ into equation A-16 and factoring out a t^2 term, we can obtain a value for s for the invariant pseudoimpulse response by solving the equation

$$\left[\sqrt{\pi}\sqrt{s/4}e^{s/4}((1/4)s^2 - 3s + 3)\text{erfc}(\sqrt{s/4}) + (s/2)(s^2 - (13/2)s + 3)\right] = 0. \quad \text{(A-17)}$$

There are two roots for equation A-17 at $s \approx 0.7$ and $s \approx 6.3$ as can be determined numerically. These correspond to two extrema in the invariant pseudoimpulse response. The global maximum corresponds to the earlier of the two extrema, and therefore, $s \approx 6.3$ for the arrival time of the invariant pseudoimpulse response.

It is important to note that, as a product, the mathematical form of the invariant and its derivatives is much more complex than the basic electric field components. However, they still behave according to a characteristic time $\tau \propto \mu\sigma[L]^2$, where L is a characteristic length scale of the problem. Although this Appendix has been concerned only with fields in a whole-space, the basic physics of the characteristic should not change when the geoelectric structure of the earth becomes more complex. Appendix B examines the variation in the scaling constant s in the case of a half-space under a finite column of seawater.

APPENDIX B

ARRIVAL TIMES IN A HALF-SPACE UNDER A FINITE COLUMN OF SEAWATER

Here, we consider the case where the electric dipole TXs and RXs lie on the seabottom, at the interface between a lower seafloor half-space of conductivity σ_1 and an upper seawater column of conductivity σ_0, and depth d. In general, the electromagnetic response cannot be derived analytically for this problem, although Edwards and Chave (1986) and Cheesman et al. (1987) examine several limiting cases in which the seawater has infinite depth and the conductivity contrast between seawater and seafloor is large. However, the general solution can be obtained quasianalytically via standard layered earth recursion relationships. Edwards (1997) gives a good overview of the algorithm required to compute the time-domain inline and broadside response of an electric dipole TX of a layered model. The invariant pseudoimpulse response can be calculated by taking the numerical derivative with respect to logarithmic time of the product of these inline and broadside fields. The peak arrival time τ can then be picked, and the scaling constant s can be calculated via

$$s = \frac{\mu\sigma_1 r^2}{\tau}, \quad \text{(B-1)}$$

where r is the TX-RX separation. It is important to note the use of the seafloor half-space conductivity in equation B-1 because we wish to subsequently use s to derive apparent resistivities of the seafloor with real data via equation 9. Typical seawater conductivity ranges from approximately 2 (0.5 Ωm) to 5 S/m (0.5 Ωm) — as observed by numerous CTD casts over multiple GEOMAR cruises — whereas seafloor conductivity could take on much larger ranges. For shallow sedimentary seafloor environments, such as mud volcanoes or gas hydrate deposits, it is unlikely that the conductivity of the upper several hundred meters of the seafloor is less than 0.1 S/m (10 Ωm). In the case of a marine mineral deposit, the conductivity of the seafloor would rarely be more than 10 S/m (0.1 Ωm).

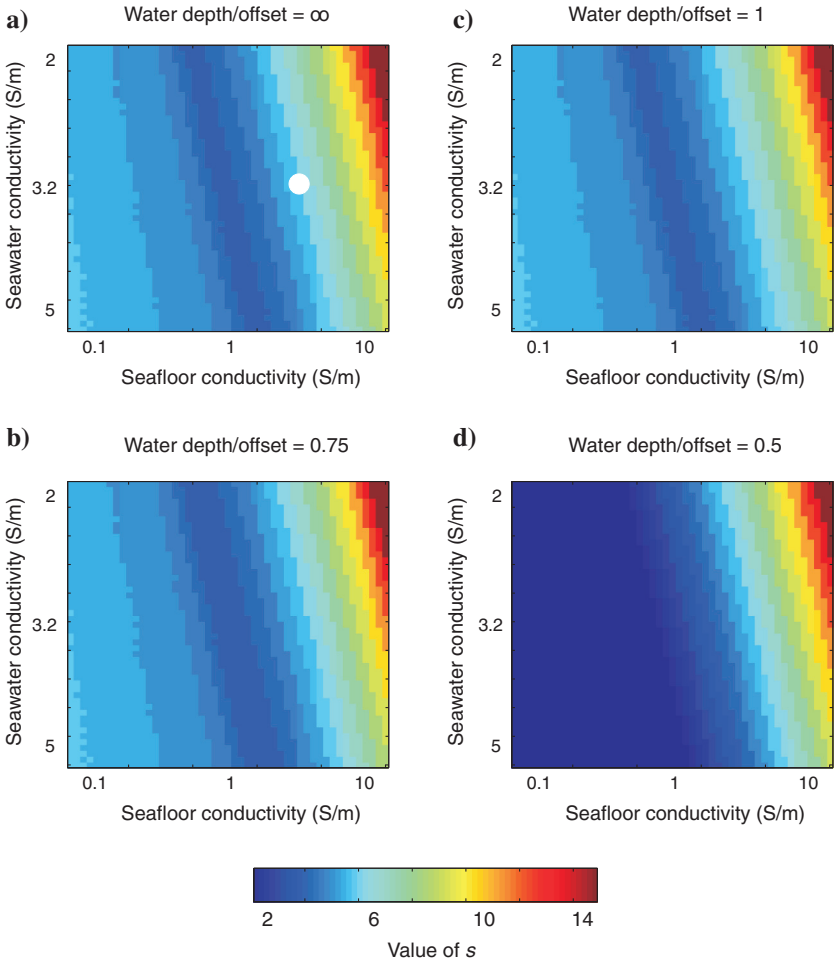

Figure B-1. Contour maps of the scaling constant s for various seawater and seafloor conductivities and water depths to offset ratios. The white dot shows an example of one case in which the conductivities are equal. Note the log scale in conductivities.

Figure B-1a shows the calculated value of s, derived via equation B-1 from synthetic pseudoimpulse response curves for a range of seafloor and seawater conductivities and an infinite water depth (in other words, a double half-space). As a cross check, when $\sigma_1 = \sigma_0$, $s \cong 6.3$, as expected by the theory in Appendix A (one example of this is indicated by the white dot in Figure B-1). In general, note that s is actually a function of the conductivity of the seafloor and, to a lesser extent, the seawater (in fact, s most likely depends on the ratio of the conductivities based on the pattern of Figure B-1). However, for seafloor conductivities near to or less than 1 S/m (1 Ωm — as would be found in a typical sedimentary seafloor environment), the value of s is approximately four, which is what we shall use for subsequent analysis of our data in this paper. Indeed, the exact choice of the scaling constant is not particularly critical because the purpose of equation 9 is to identify variations on the seafloor resistivity structure, as opposed to absolute values. For a seafloor that is more resistive than the seawater, s increases slightly as the resistivity of the seafloor increases. From equation 9, this implies that the apparent resistivity will be slightly overestimated when the seafloor is on the order of 0.1 S/m (10 Ωm) or less.

The large values of s observed when the seafloor is more conductive than the seawater are due to the change in physics; the diffusion velocity in the seawater is now higher than in the seafloor, and therefore the invariant pseudoimpulse response has a different character. The main peak is now a function of seawater resistivity as opposed to seafloor resistivity, and therefore, it is questionable if the imaging method we present here is suitable for a conductive seafloor. This does not mean that the survey described in Figure 2 is not suitable for conductive targets, but rather that an alternative method of imaging the data may be necessary for such scenarios.

The remaining three panels in Figure B-1 show the same analysis for the case of finite water depth. When the water depth is equal to or greater than the TX-RX offset, the fields are hardly distorted by the seawater-air interface, and therefore the values of s are the same as those for infinite water depth. As the water depth approaches 0.75 times the offset, the effect of the airwave starts to be a factor, and the values of s are modified to some extent. Once the water depth is half the TX-RX offset, the fields are more strongly distorted by the airwave and the values of s are significantly affected. However, note that for a given seafloor and seawater conductivity, the value of s in shallow water is less than the value of s in deep water — an effect likely due to the destructive interference between the signals arriving through the air and through the subsurface. From equation 9, this implies that the apparent resistivity will typically be underestimated using a value of $s = 4$ when the water depth approaches half the TX-RX offset. In the case of the WND, the water depth was approximately 500 m and the maximum TX-RX offset was approximately 1000 m. This suggests that the increased resistivities at the center of the mud volcano are actually underestimated given the assumption of infinite water depth. Again, regardless of the exact choice of s, the purposes of our approach are to quality control our data and to highlight areas of anomalous resistivity in the seafloor with this simple mapping tool.

REFERENCES

Archie, G. E., 1942, The electrical resistivity log as an aid in determining some reservoir characteristics: Journal of Petroleum Technology, **5**, 1–8, doi: 10.2118/942054-G.

Bialas, J., D. Kläschen, C. Papenberg, R. Gehrmann, and M. Sommer, 2010, 3-D seismic images of mud volcano North Alex, West-Nile Delta, Egypt: Presented at European Geophysical Union General Assembly.

Bibby, H., 1977, The apparent resistivity tensor: Geophysics, **42**, 1258–1261, doi: 10.1190/1.1440791.

Bibby, H., 1986, Analysis of multiple-source bipole-quadripole resistivity surveys using the apparent resistivity tensor: Geophysics, **51**, 972–983, doi: 10.1190/1.1442155.

Cairns, G., R. Evans, and R. N. Edwards, 1996, A time domain electromagnetic survey of the TAG hydrothermal mound: Geophysical Research Letters, **23**, 3455–3458, doi: 10.1029/96GL03233.

Caldwell, T., and H. Bibby, 1998, The instantaneous apparent resistivity tensor: A visualization scheme for LOTEM electric field measurements: Geophysical Journal International, **135**, 817–834, doi: 10.1046/j.1365-246X.1998.00668.x.

Cheesman, S. J., R. N. Edwards, and A. D. Chave, 1987, On the theory of sea-floor conductivity mapping using transient electromagnetic systems: Geophysics, **52**, 204–217, doi: 10.1190/1.1442296.

Constable, S., 2010, Ten years of marine CSEM for hydrocarbon exploration: Geophysics, **75**, no. 5, A67–A81, doi: 10.1190/1.3483451.

Constable, S., and C. S. Cox, 1996, Marine controlled-source electromagnetic sounding. Part 2: The PEGASUS Experiment: Journal of Geophysical Research, **101**, 5519–5530, doi: 10.1029/95JB03738.

Domenico, S. N., 1977, Elastic properties of unconsolidated porous sand reservoirs: Geophysics, **42**, 1339–1368, doi: 10.1190/1.1440797.

Dupre, S., J. Woodside, J. P. Foucher, G. de Lange, J. Mascle, A. Boetius, V. Mastalerz, A. Stadnitskaia, H. Ondreas, C. Huguen, F. O. Harmegnies, S. Gontharet, L. Loncke, E. Deville, H. Niemann, E. Omoregie, K. O.-L. Roy, A. Fiala-Medioni, A. Dahlmann, J. C. Caprais, A. Prinzhofer, M. Sibuet, C. Pierre, J. S. S. Damste, and N. S. Party, 2007, Seafloor geological studies above active gas chimneys off Egypt (Central Nile deep sea fan): Deep-Sea Research Part I: Oceanographic Research Papers, **54**, 1146–1172, doi: 10.1016/j.dsr.2007.03.007.

Edwards, R. N., 1997, On the resource evaluation of marine gas hydrate deposits using sea-floor transient electric dipole-dipole methods: Geophysics, **62**, 63–74, doi: 10.1190/1.1444146.

Edwards, R. N., and A. D. Chave, 1986, A transient electric dipole-dipole method for mapping the conductivity of the sea floor: Geophysics, **51**, 984–987, doi: 10.1190/1.1442156.

Ellingsrud, S., T. Eidesmo, S. Johansen, M. Sinha, L. MacGregor, and S. Constable, 2002, Remote sensing of hydrocarbon layers by seabed logging SBL: Results from a cruise offshore Angola: The Leading Edge, **21**, 972–982, doi: 10.1190/1.1518433.

Feseker, T., K. Brown, C. Blanchet, F. Scholz, M. Nusso, A. Reitz, M. Schmidt, and C. Hensen, 2010, Active mud volcanoes on the upper slope of the western Nile deep-sea fan — First results from the P362/2 cruise of R/V Poseidon: Geo-Marine Letters, **30**, 169–186, doi: 10.1007/s00367-010-0192-0.

Feseker, T., A. Daehlmann, J. P. Foucher, and F. Harmegnies, 2009, In-situ sediment temperature measurements and geochemical pore-water data suggest highly dynamic fluid flow at Isis mud volcano, eastern Mediterranean Sea: Marine Geology, **261**, 128–137, doi: 10.1016/j.margeo.2008.09.003.

Gontharet, S., C. Pierre, M. M. Blanc-Valleron, J. M. Rouchy, Y. Fouquet, G. Bayon, J. P. Foucher, J. Woodside, and J. Mascle, , The Nautinil Scientific Party, 2007, Nature and origin of diagenetic carbonate crusts and concretions from mud volcanoes and pockmarks of the Nile deep-sea fan (eastern Mediterranean): Deep-Sea Research Part II, **54**, 1292–1311, doi: 10.1016/j.dsr2.2007.04.007.

Hallof, P., 1964, A comparison of the various parameters employed in the variable-frequency induced-polarization method: Geophysics, **29**, 425–433, doi: 10.1190/1.1439376.

Hensen, C., M. Nuzzo, E. Hornibrook, L. M. Pinheiro, B. Bock, V. H. Magalhaes, and W. Brückmann, 2007, Sources of mud volcano fluids in the Gulf of Cadiz — Indications for hydrothermal imprint: Geochimica et Cosmochimica Acta, **71**, 1232–1248, doi: 10.1016/j.gca.2006.11.022.

Hölz, S., A. Swidinsky, M. Sommer, M. Jegen, and J. Bialas, 2015, The use of rotational invariants in the interpretation of marine CSEM data: Geophysical Journal International, doi: 10.1093/gji/ggv015.

Kopf, A., 2002, Significance of mud volcanism: Reviews of Geophysics, **40**, 1–52, doi: 10.1029/2000RG000093.

Loke, M. H., and R. D. Barker, 1996, Rapid least-squares inversion of apparent resistivity pseudo-sections using quasi-Newton method: Geophysical Prospecting, **48**, 131–152, doi: 10.1111/j.1365-2478.1996.tb00142.x.

O'Suilleabhain, L., M. Rosenquist, J. Johnson, R. E. Plessix, R. Van Rensburgen, and D. Sebayang, 2012, Anisotropic inversion of CSEM data from offshore Malaysia: 82nd Annual International Meeting, SEG, Expanded Abstracts, doi: 10.1190/segam2012-0726.1.

Risk, G. F., H. M. Bibby, and T. G. Caldwell, 1993, DC resistivity mapping with the multiple-source bipole-dipole array in the Central Volcanic Region, New-Zealand: Journal of Geomagnetism and Geoelectricity, **45**, 897–916, doi: 10.5636/jgg.45.897.

Schwalenberg, K., E. C. Willoughby, R. Mir, and R. N. Edwards, 2005, Marine gas hydrate signatures in Cascadia and their correlation with seismic blank zones: First Break, **23**, 57–63.

Sommer, M., S. Hölz, M. Moorkamp, A. Swidinsky, B. Heincke, C. Scholl, and M. Jegen, 2013, GPU parallelization of a three dimensional marine CSEM code: Computers and Geosciences, **58**, 91–99, doi: 10.1016/j.cageo.2013.04.004.

Streich, R., and M. Becken, 2010, Electromagnetic fields generated by finite-length wire sources: Comparison with point dipole sources: Geophysical Prospecting, **59**, 361–374, doi: 10.1111/j.1365-2478.2010.00926.x.

Swidinsky, A., and R. N. Edwards, 2010, The transient electromagnetic response of a resistive sheet: An extension to three-dimensions: Geophysical Journal International, **182**, 663–674, doi: 10.1111/j.1365-246X.2010.04649.x.

Swidinsky, A., S. Hölz, and M. Jegen, 2013, Rapid resistivity imaging using a transient marine CSEM survey with two transmitter polarizations: 75th Annual International Conference and Exhibition, EAGE, Extended Abstracts, Tu 11 11.

Ward, S. H., and G. W. Hohmann, 1988, Electromagnetic theory for geophysical applications, *in* M. N. Nabighian, ed., Electromagnetic methods in applied geophysics, vol. 1, SEG, 131–311.

Weitemeyer, K., S. Constable, K. Key, and J. Behrens, 2006, First results from a marine controlled-source electromagnetic survey to detect gas hydrates offshore Oregon: Geophysical Research Letters, **33**, L03304, doi: 10.1029/2005GL024896.